Enhancement of single particle rare earth doped $NaYF_4$: Yb, Er emission with a gold shell

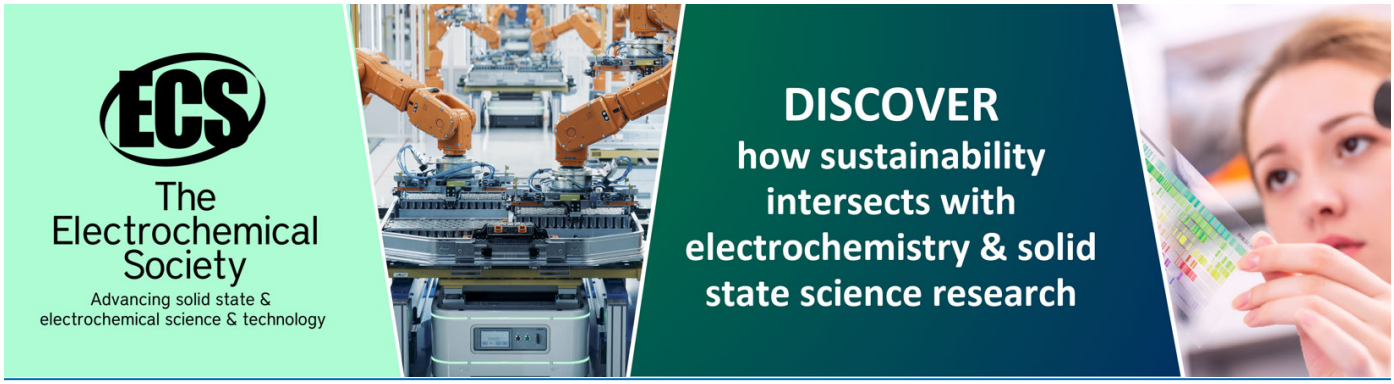

OPEN ACCESS
IOP Publishing
Nanotechnology

Nanotechnology **26** (2015) 025101 (9pp)
doi:10.1088/0957-4484/26/2/025101

Enhancement of single particle rare earth doped $NaYF_4$: Yb, Er emission with a gold shell

Ling Li, Kory Green, Hans Hallen and Shuang Fang Lim

Department of Physics, North Carolina State University, Raleigh, NC 27695, USA

E-mail: sflim@ncsu.edu

Received 27 July 2014, revised 10 November 2014
Accepted for publication 12 November 2014
Published 17 December 2014

Abstract

Upconversion of infrared light to visible light has important implications for bioimaging. However, the small absorption cross-section of rare earth dopants has limited the efficiency of these anti-Stokes nanomaterials. We present enhanced excitation absorption and single particle fluorescent emission of sodium yttrium fluoride, $NaYF_4$: Yb, Er based upconverting nanoparticles coated with a gold nanoshell through surface plasmon resonance. The *single* gold-shell coated nanoparticles show enhanced absorption in the near infrared, enhanced total emission intensity, and increased green relative to red emission. We also show differences in enhancement between single and aggregated gold shell nanoparticles. The surface plasmon resonance of the gold-shell coated nanoparticle is shown to be dependent on the shell thickness. In contrast to other reported results, our single particle experimental observations are corroborated by finite element calculations that show where the green/red emission enhancement occurs, and what portion of the enhancement is due to electromagnetic effects. We find that the excitation enhancement and green/red emission ratio enhancement occurs at the corners and edges of the doped emissive core.

S Online supplementary data available from stacks.iop.org/NANO/26/025101/mmedia

Keywords: bioimaging, upconversion, near infrared

(Some figures may appear in colour only in the online journal)

Introduction

Contrast agents play an important role in the study of biological tissues and whole organisms, since they enable visualization of functional structures. Fluorescent contrast agents also enable specific targeting in therapeutic approaches. Developing optimized contrast agents is central to optimizing the performance of both imaging and therapy. The ideal contrast agent for optical microscopy combines high resolution, specific targeting of functional groups, 3D imaging (depth resolution), low toxicity, low bleaching (long observation time at high signal), and high signal to noise (low background). Traditional organic dyes and fluorescent proteins are excited in the ultraviolet (UV) or blue spectral region, and emit at a longer-wavelength [1] that is Stokes-shifted [2]. The use of the short-wavelength excitation leads to a short penetration depth of the excitation light [3] and gives rise to autofluorescence, photobleaching and photodamage to biological specimens [4]. It is thus primarily suited to pathological and *in vitro* imaging, but has limited applicability to live imaging. In contrast, near-infrared (NIR) multiphoton microscopy offers high penetration depth and high spatial and temporal resolution, with low autofluorescence backgrounds [5–7]. However, conventional two-photon microscopy, using two-photon dyes, requires high excitation densities (10^6–10^9 W cm^{-2}) attributed to the simultaneous

absorption of two coherent NIR photons, and as a result, expensive pulsed lasers are required. Imaging using UCNPs combines conceptual strengths of both fluorescence microscopy and two-photon imaging, while avoiding common drawbacks. The upconversion mechanism is based on either sequential excitation of the same emitting center in II–VI semiconductor upconverters [8–12], dyes [13–15], and singly doped rare earth ion upconverters [16, 17], or excitation of two centers and subsequent energy transfer in co-doped rare earth upconverters [18–20]. However, there are fundamental differences between the semiconductor upconverters and the lanthanide doped upconverters emphasized in this study. One is that upconversion in the former operates via a virtual, or weakly allowed intermediate state. Hence, upconversion luminescence lifetimes are on the order of tens of nanoseconds compared to hundreds of microseconds in lanthanide doped upconverters which operate via real, long-lived intermediate states. In practical terms, this mean that semiconductor upconverters are more efficiently excited by nanosecond pulsed laser sources while lanthanide doped upconverters are efficiently excited by continuous wave (CW) sources.

In the co-doped rare earth ion upconverter system studied here, the ytterbium and erbium dopant couple, the upconversion occurs through an energy transfer upconversion process, where the Yb^{3+} ion transfers its energy to the Er^{3+} ion [18]. Hence, imaging using UCNPs exploits the low excitation intensity of fluorescence microscopy, such as that provided by a more affordable CW diode laser, while retaining the benefits of the large penetration depth and background of two-photon fluorescence [21–23]. These materials have been investigated for their bio-applications, as reporters for immunoassay [24–31], biolabels [32–34], bio-therapy [35–40] and spectral conversion in solar cells [41–46], where they increase the absorption of sub-bandgap light.

Despite using a real rather than virtual intermediate state, the brightness and upconversion efficiency of these nanoparticles is not comparable to that of semiconductor nanoparticles and dyes. The down-scaling of particle size that is needed to promote bio-distribution and the body clearance of such ultra-small nanoparticles [47] also leads to a rapid loss of brightness. This has been attributed to the low absorption cross-section of the rare earth ion dopants. That is because transitions to the inner 4f-shell levels in rare earth ions are only very weakly allowed; hence their absorption coefficients are very small, limiting their maximum emission intensities [48]. Various strategies employed to increase emission intensities include co-doping with lithium ions [49–52], gadolinium ions [19, 53–55], transition metals [56] and growth of a protective shell [57] Although that shortcoming is partially compensated by its zero background fluorescence and its non-blinking and non-bleaching properties, we show that plasmonics can increase the absorption and emission efficiencies.

The coupling of Stokes type fluorescent emitters to metallic surfaces and nanoparticles has been shown to modify both the excitation and emission [58–63]. This effect has been abundantly demonstrated by coupling of semiconductor nanoparticles to gold films, gold nanoparticles and gold shells. Recently, there has been interest in enhancing anti-Stokes emission by coupling gold and silver nanoparticles and shells to rare earth ion doped upconverting cores [20, 64–67], resulting in modified overall emission intensity, modification of the relative green over red emission [20, 64, 66–69] and opening up possibilities of bimodal imaging [20]. The enhancement is attributed to the tuning of the surface plasmon resonances to be closer to the excitation of the rare earth doped core. However, few groups other than Schietinger *et al* [64], have investigated the effect of gold coupling to upconverter cores at the *single* particle level and correlated the enhancement with a model. The study of single particles is important as it eliminates aggregation effects in particle clusters, where the closely spaced nanoparticles have a modified electric field distribution and thus different enhancement characteristics. The in-depth study of upconverted single particle fluorescence is also critical for their development as single molecule fluorescent probes [23, 70], where they have shown that samples optimized for bright emission in ensemble measurements are in fact dim under the tightly focused excitation in single particle imaging, while samples optimized for bright emission under single particle excitation, are dim under the low excitation powers used in ensemble measurements. Investigation of the enhancement at the single particle level is directly relevant to this work because we can explain both quantitatively and qualitatively the effect of the gold shell. The single particle results are also more consistent with our finite element calculations, without having to correct for anomalies generated by ensemble measurements. The finite element calculations show where the green/red emission enhancement occurs, and what portion of the enhancement is due to electromagnetic effects.

In this work, an undoped 60 nm thick sodium yttrium fluoride shell, followed by a silica spacer has been added to the hexagonal plate shaped, doped center to reduce emission quenching by the gold layer, and also to reduce the influence of the gold shell on the transition rates of the rare earth emitters, so that we can focus on the increased energy absorption due to the influence of the gold shell. The gold shell thickness was modified to tune the surface plasmon resonance peak to the near infrared region, resonant with the Yb^{3+}/Er^{3+} dopant couple. After optimization, we have successfully observed emission intensity enhancement of the gold-shell nanoparticles. Our finite element calculations corroborate the measured intensity enhancements and are in agreement with experimental results seen in more spherical shaped gold-shell nanoparticles studied by other groups [20, 64–66, 71]. We have measured the emission of *single* nanoparticles, as this will minimize changes in the electric field distribution when gold-shell nanoparticles are placed close together [72]. We demonstrate the importance of this by presenting, the fluorescence image and upconverted spectral data of two gold-shell nanoparticles in close contact. When in close contact, they display a drop in the overall emission intensity and also a reduction of green compared to red emission intensity. Hence, despite the immense fluorescence enhancement that can be attained by tuning the resonant

excitation, aggregation effects must be carefully minimized. We speculate that the failures of many efforts at enhancement using the gold shell strategy are, in fact, due to aggregation effects. Additionally, in this work we have suspended our gold-shell nanoparticles in a spin-on-glass substrate to immobilize them, enabling single particle measurements, and reducing orientation effects resulting from the asymmetry of our nanoparticle shape [73]. We demonstrate through both our experiments and calculations that the gold shell thickness influences the relative enhancement of the green and red emissions. Finally, ours is the first study to show that upconversion emission is enhanced at the corners and edges of the hexagonal plate shaped nanoparticle.

Methods

The doped core and un-doped shell were grown in a two-step process. For growth of the doped core, 2.1 mmol of sodium trifluoroacetate, 0.78 mmol of yttrium trifluoroacetate, 0.199 mmol of ytterbium trifluoroacetate, and 0.018 mmol of erbium trifluoroacetate were combined in 6.2 ml of oleic acid and 6.3 ml of octadecene. The mixture was heated at 120 °C for 30 min, after which, the temperature was increased to 330 °C for 55 min for core growth. After cooling, the doped nanocrystals were precipitated and washed 6 times with ethanol, and dried under filtered air flow.

For undoped shell growth, 2.1 mmol of sodium trifluoroacetate and 1 mmol of yttrium trifluoroacetate are added to 6.2 ml of oleic acid and 6.3 ml of octadecene. The mixture was heated to 120 °C for 30 min, and the core nanocrystals obtained earlier were added, and heated at 120 °C for another 30 min. The temperature was then raised to 330 °C and held for 30 min followed by a temperature reduction to 280 °C for 25 min, for growth of the undoped shell. After cooling, the doped core/undoped shell nanoparticles were precipitated and washed 6 times with ethanol, and dried under filtered air flow.

For the silica coating of the nanoparticles, 0.15 g of the doped core/undoped shell nanoparticles were mixed with 2 ml of CO-520 surfactant in 200 ml of cyclohexane and sonicated for 10 min. After that, a further 8 ml of CO-520 and 1.6 ml of concentrated ammonia were added and sonicated for a further 20 min or until the dispersion turns clear. Then, 800 μl of tetraethyl orthosilicate was slowly added while stirring, and the mixture was left stirring for two days. The nanoparticles were precipitated with acetone, and washed 6 times with ethanol.

For the amine functionalization of the silica surface, 0.06 g of the silica coated nanoparticles were dispersed in 85 ml of ethanol by sonication. Then, 640 μl of concentrated ammonia was added with a 20 min sonication. After that, 46.5 μl of 3-aminopropyltriethoxysilane was slowly added and the dispersion was left to stir for 24 h. The dispersion was next heated at a reflux temperature of roughly 78 °C for 2 h. When cooled, the nanoparticles were centrifuged and washed at least 6 times with ethanol, and an additional 2 times with a buffer at pH 6.

For the formation of Au seeds, 4.96 μl of 80% tetrakis (hydroxymethyl) phosphonium chloride was dispersed in 17 ml of ultrapure water and 0.6 ml of 0.2 M NaOH with sonication for 20 min. After that, 2 ml of 0.01 M chloroauric acid ($HAuCl_4$) was added and immediately a dark brown solution was observed. Immediately, 0.03 g of $NaYF_4$ nanoparticles were vortexed in 20 ml of the Au seed solution for about 30 min and left overnight without stirring at 25 °C in the dark. The $NaYF_4$/Au seeded nanoparticles were centrifuged and washed at least 6 times with centrifugation in ultrapure water.

For Au shell growth, 10 mg of potassium carbonate was dissolved in 8.5 ml of ultrapure water by sonication for 10 min. About 1.5 ml of 0.01 M $HAuCl_4$ was then added. About 1 ml of this potassium carbonate/Au solution was then topped up to 4 ml with 3 ml of ultrapure water. This was followed by addition of 0.00375 g of the $NaYF_4$/Au seed nanoparticles (first dispersed in 200 μl of ultrapure water) and 10 μl of 35% formaldehyde as a reducing agent. The nanoparticles were maintained at 25 °C in the dark for growth of the Au shell, while Au shell growth was evaluated at 2–5 min intervals by UV–vis absorption measurements. After each growth interval, a sample of the nanoparticles were washed with centrifugation at least 6 times with ultrapure water. TEM measurements were performed on the unmodified nanoparticle, silica modified nanoparticles and Au shell modified nanoparticles to obtain the thickness of each grown layer.

For the dispersion of the nanoparticles in a thin film, roughly 0.003 75 g of the nanoparticles were mixed in 0.72 g of sodium metasilicate (about 300 μl) and sonicated for 20 min. About 100 μl of the dispersion was pipetted onto clean microscope slides and left to dry under filtered air flow.

TEM images were performed on a JEOL 2000FX TEM at the Analytical Instrumentation Facility on the NC State University Campus. UV–vis spectra were collected on a Varian, Cary 50 Scan, UV–vis spectrophotometer. Single particle upconverted emission spectra were collected on a Nikon TE-2000U microscope, using an Ocean Optics USB2000+ spectrometer. A Qphotonics QSP-975-6 collimated diode laser, coupled into the microscope, and focused with a 20X objective of N.A. 0.4, provided the excitation for the upconverted spectra. Assuming the full fill of the lens diameter by the near infrared illumination, the modified theoretical diffraction limited spatial resolution which is achievable using an optical microscope, the radius of the focal spot over a single gold-shell nanoparticle is, 980 nm/(2 X N. A.) = 1.225 μm. As the measured average excitation is at 30 mW, the incident power density is about 6.3×10^8 mW cm^{-2}, which is over the saturation threshold of 8000 mW cm^{-2} observed by Suyver *et al* [74]. Hence, the measured emission is assumed to be linear with the excitation power. A CCD camera connected to a microscope port was used to record the fluorescence image to confirm the presence of single nanoparticles or aggregates.

Finite element analysis was used for the computational results. The angular average electrical field amplitude for optimal gold shell thickness modeling was calculated for 15 point sites: three radial and three depth, along two symmetry

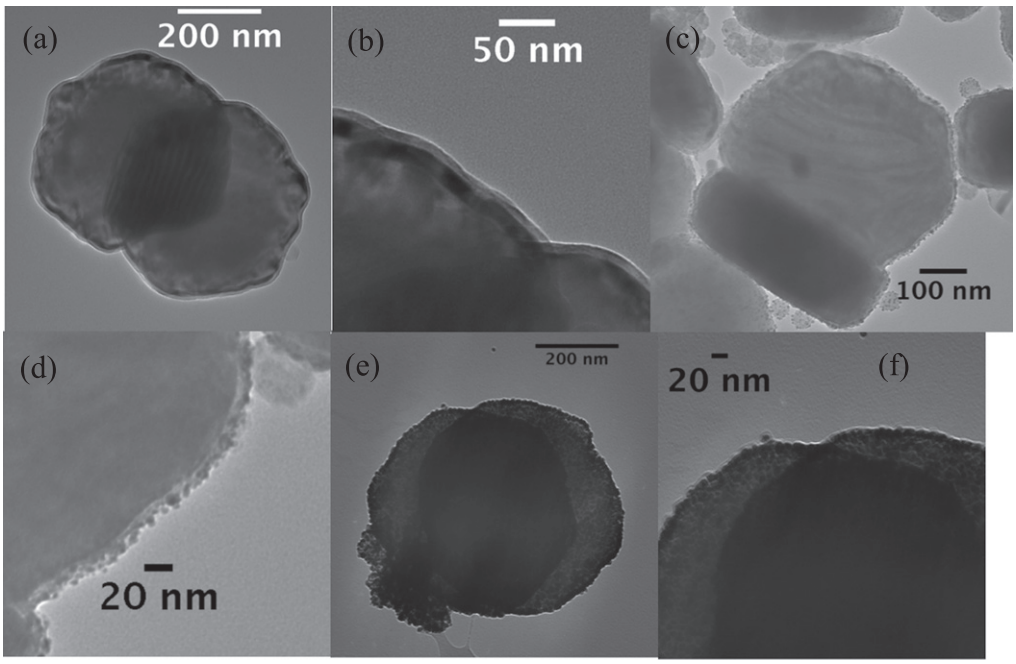

Figure 1. (a) TEM image of the $NaYF_4$: Yb^{3+}, Er^{3+} center (335 nm)/undoped $NaYF_4$ shell (60 nm)/silica–amine shell (10 nm), (b) view of the silica–amine shell, (c) with 3–5 nm diameter gold seeds attached on the silica–amine surface and (d), view of the gold seeds, (e) growth of a gold shell (10–11 nm), and (f) view of the gold shell.

directions within the doped core. The emission spectra from 500 nm to 700 nm were modeled with single point electric dipoles of unit dipole moment and different polarizations, at the same 15 locations inside the doped core. These spectra were scaled by the excitation enhancement factor at that location and the measured spectrum without gold shell. The final emission spectrum was obtained by weighted averaging these spectra over dipole locations and polarizations. In our single particle measurements, the pump power intensity was high enough such that we are well within the saturation emission regime of the nanoparticles. In the saturation regime, the relationship between emission intensity and pump power intensity is linear [74]. We made that assumption in our emission calculations, and also the additional assumption of equal green and red emission power at saturation [75].

Results

The TEM image in figures 1(a) and (b) shows the upconverting nanoparticle modified with a silica/amine shell, consisting of a 335 nm diameter (from point to point of the hexagon) and of 180 nm in height, doped upconverting center, surrounded by a 60 nm thick undoped shell to form the core and a 10 nm thick silica–amine shell. We refer to an uncoated or core nanoparticle as one consisting of just the doped center and undoped shell. Figures (c) and (d) shows gold seed attachment, where an initial high density of ultra small sized gold seed attachment was needed, since enhancement by surface plasmon resonance takes place over a very narrow range of gold shell thicknesses. Finally, figures (e) and (f) shows growth of gold seeds into a 15 nm thick gold shell. We specifically chose such a thick, 60 nm, undoped shell to minimize quenching by gold. It also simplifies analysis by reducing the influence of the gold shell on the transition rates of the rare earth emitters from significant modification by nearby gold. Hence, the results from core nanoparticles without gold can be used without modification for first level models. Too thick a gold shell blocks both excitation and emission.

We have monitored the shift in surface plasmon resonance energy as the gold shell grows. The absorption spectra in figure 2, shows the resultant peak shifts with gold shell growth time up to 21 min. At 1 min, each gold seed has grown in size, but they are still independent, so we observe a plasmon peak at 525 nm, which is typically associated with gold nanoparticles. With further growth, neighbors get closer, and the seeds coalesce to form partial shells, accompanied by a gradual red-shift of the surface plasmon peak. At 10 min, a 10–11 nm thick gold shell has been observed. Longer growth time of 15 and 20 min, results in a shell thickness of ~15 nm and 18–20 nm, respectively. The observed data in figure 2 is that of an ensemble of gold-shell nanoparticles, under Brownian motion, with each nanoparticle randomly oriented in solution. Since our nanoparticles are large and of hexagonal plate shape, they are optically anisotropic, and there is a stronger surface plasmon resonance dependence on nanoparticle orientation as compared to uniformly spherical shaped nanoparticles [73]. This is reflected in the broadened plasmon resonance peaks shown in this UV–vis data.

Figure 3 shows the upconverted emission spectra of a single gold-shell nanoparticle (*the single gold shell particle upconverted fluorescence image taken at* 20*X magnification is shown inset*). Upconverted emission peaks were observed at

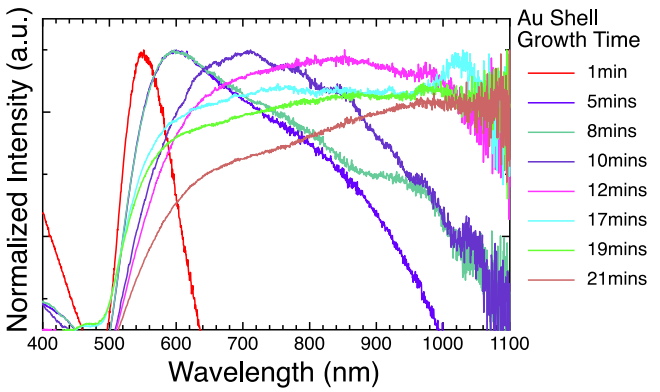

Figure 2. UV–vis absorption spectra of the $NaYF_4$: Yb^{3+}, Er^{3+} center (335 nm)/$NaYF_4$ shell (60 nm)/silica–amine shell (10 nm) as the gold nanoshell is formed on the surface.

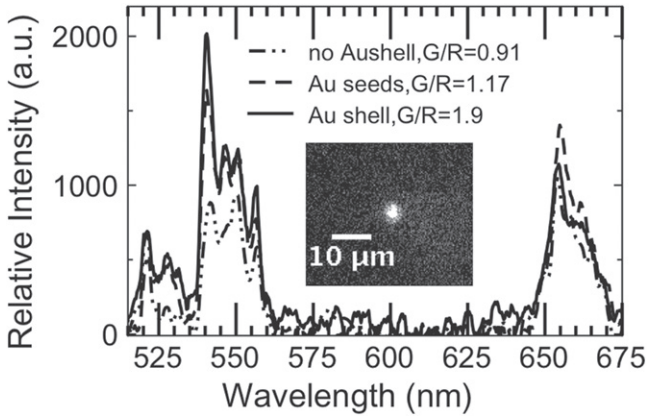

Figure 3. Single particle upconverted emission at 980 nm excitation of upconverting core with no gold shell (dotted line), with gold seeds only (dashed line) and with a 10–11 nm thick gold shell (bold line). (Inset) upconverted emission image of the measured gold-shell nanoparticle.

around 525 nm, 550 nm, and 655 nm, which are attributed to the following levels, $^2H_{11/2}$, $^4S_{3/2}$ and $^4F_{9/2}$, respectively. The emission spectra shows a relative green (550 nm)/red (655 nm) emission ratio of roughly 0.9 for the uncoated core nanoparticles and remains consistent over a large number of measured nanoparticles. For gold-seed coated nanoparticles, the green emission exhibits an increase, by 1.9 times, with the green/red ratios varying from 1.0 to 1.3 over the measured nanoparticles. In addition, we also observe that, unlike the uncoated nanoparticles, when gold shell coated nanoparticles are aggregated, as shown in figure 4, total emission intensity and green/red ratios are reduced. The green/red ratios vary from 0.4 to 0.9 for cases in which two or more such nanoparticles are in close contact.

As a gold shell of up to 15 nm thickness is grown on the upconverting core nanoparticles, the green emission increases again to about 2.3 times that of the uncoated nanoparticles, accompanied by another increase in green/red ratio to about 1.9. Just as in the case of gold-seed coated nanoparticles, their green/red ratios are not constant from sample to sample, but instead are observed to vary from 1.1 up to 2.0. We believe that the variability in the observed green/red ratios can be

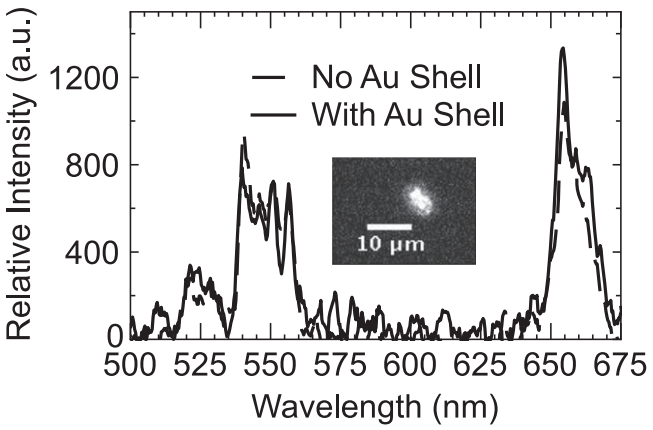

Figure 4. Upconverted emission of aggregate at 980 nm excitation of $NaYF_4$: Yb^{3+}, Er^{3+} center (335 nm)/$NaYF_4$ shell (60 nm)/silica–amine shell (10 nm) with 10–11 nm Au shell (solid line) and no Au shell (dash and solid line), (inset) upconverted emission image of aggregated gold-shell nanoparticles.

attributed to the orientation of individual hexagonal plate shaped gold-shell nanoparticles with respect to that of the incoming near infrared excitation [73]. When two such nanoparticles are in close contact, emission quenching takes place [72], and green/red ratios fall to the 0.6–0.9 range.

Discussion

Several of these observations can be understood by finite element modeling. Figure 5 documents these observations, showing the spatial dependence of the electric field at four combinations of incident light direction, excitation polarization and nanocrystal orientation. In the figure, the most strongly enhanced configurations are the ones with light incident perpendicular to the top face with hexagonal shape and polarized either from apex to apex or the flat to flat sides (figures 5(a) and (c)). The enhancement with light incident in the plane of the hexagon is smaller.

Figure 6 shows the average electric field dependence on gold shell thickness. Our calculations show that the optimal field enhancement occurs at a shell thickness of 10 nm, compared to that of the measured optimal shell thickness of 15 nm from TEM. Our model assumes a perfect, dense and continuous Au shell, whereas experimentally, growth from seeds yields a slightly discontinuous shell structure. Effective medium theory can more accurately represent the gold shell, and explain this discrepancy. The thicker but void-containing experimental film would be electromagnetically comparable to the thinner, perfect film used in the model. In particular, we calculate the expected measured thickness t_{exp} by requiring the same propagation loss for light passing through the perfect model film t_{Au} as through the imperfect film by setting the Beer's law exponents to be the same, $n_{i,Au}\, t_{Au} = n_{i,eff}\, t_{exp}$, with gold dielectric constant at 960 nm [76], $(n_{r,Au} + n_{i,Au})^2 = -46.797 + 3.0i$ and the modeled thickness $t_{Au} = 10$ nm. We use the Bruggeman effective medium theory, valid for inclusions that may be connected [77], to obtain the effective index of

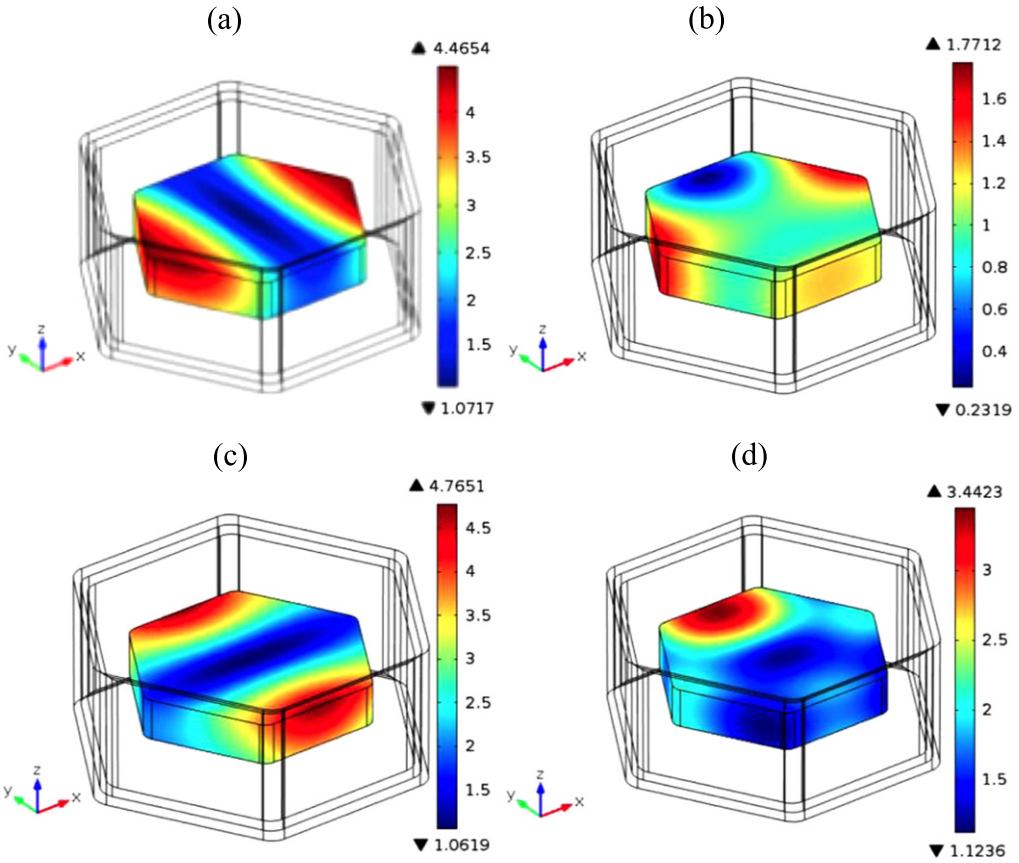

Figure 5. Four different relative configurations between the incident light direction, excitation polarization and nanocrystal orientation. (a) The light is incident from above the plate with polarization apex–apex (the red ones). (b) The incident light is polarized vertically and enters towards the red apex. (c) The light incident from above is polarized face–face (perpendicular to the red faces). (d) The light incident towards the red face is polarized vertically.

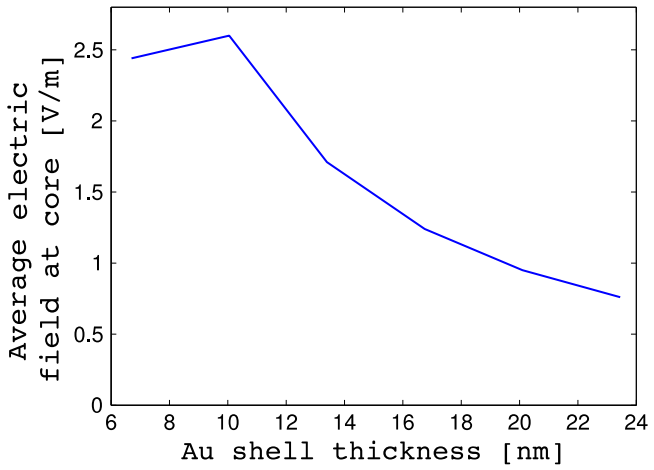

Figure 6. Average electric field within the UCNP core as a function of the Au shell thickness.

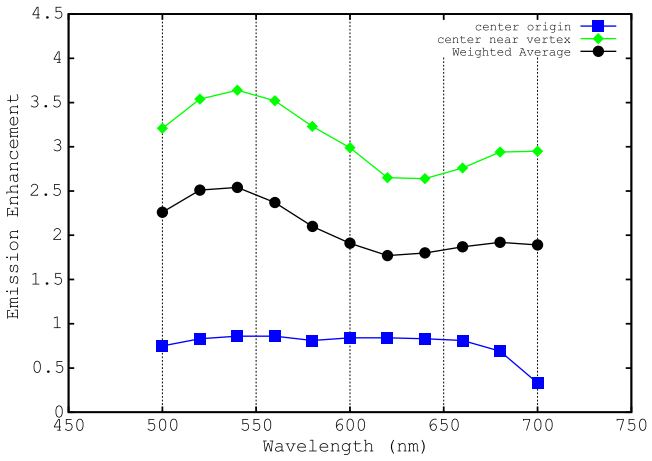

Figure 7. Total averaged emission enhancement of a single gold-shell nanoparticle, from 500 nm to 700 nm for an optimal gold shell thickness of 10 nm is compared to the emission enhancements at several specific dipole source locations.

the real film, $n_{r,eff} + n_{i,eff}$, using the gold dielectric constant, the sodium metasilicate (medium) index of refraction of 1.52, and the gold volume fraction estimated from the transmission electron micrographs to be 0.6, which is close to the closest packed spheres in one layer value. The result for the expected measured thickness $t_{exp} = 17.7$ nm, which is in reasonable agreement with the measured 15 nm given the uncertainty in the volume fraction measurement ($t_{exp} = 15$ nm is given by a 0.666 volume fraction).

Figure 7 shows the ratio of the emitted power to the total dipole power (measured on a surface within the cavity) of a single gold-shell nanoparticle calculated for each dipole position and wavelength, from 500 nm to 700 nm, and scaled

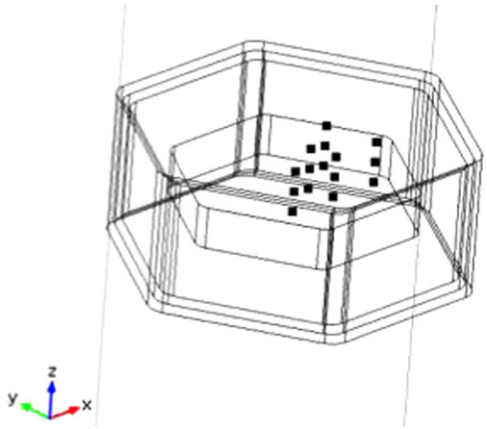

Figure 8. Schematic of the chosen 15 dipole positions within the upconverting center.

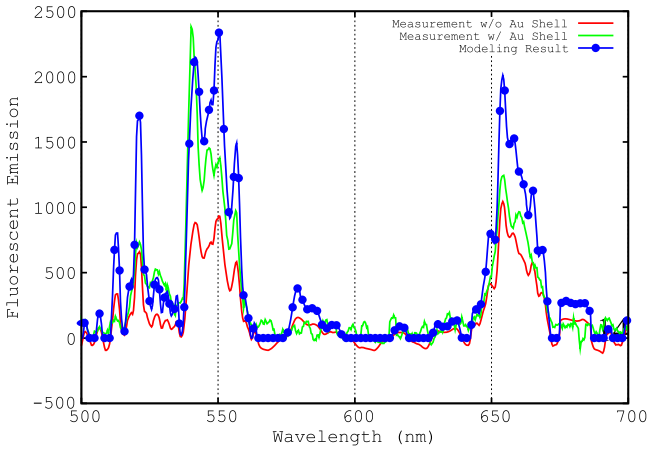

Figure 9. Modeled emission spectrum of the gold-shell nanoparticles plotted against the experimental spectra for uncoated nanoparticles for comparison.

by the excitation enhancement at that point. An optimal shell thickness of 10 nm is used. The overall average spectrum was obtained by a radius-weighted average over the 15 dipole locations, as shown in figure 8, and two orthogonal polarization directions within the doped nanocrystal core. The weighting accounts for the greater volume of nanocrystal at larger distances from the center. The calculations show an intensity enhancement for green 550 nm emission of ~2.6 times, which is comparable to the measured intensity enhancement of ~2.3 times. The discrepancy can be attributed to the assumption of a perfect continuous gold shell, the number of dipoles modeled, and the accuracy of the dielectric constants used.

The green/red emission ratio is near 1 for an uncoated nanoparticle, whereas the measured ratio for our gold-shell coated nanoparticles is found to be ~1.9. The results in figure 9 indicate that finite element calculations can explain some of this increase. The emission spectrum was obtained by scaling the spectrum of an uncoated nanoparticle by the position-dependent, polarization and emission angle averaged, unit strength dipole spectrum, and by the position-dependent excitation power. The emission angles were limited to those captured by a collection lens similar to that used in the experiment, and an optimal nanoparticle orientation was used, since the brightest nanoparticles were chosen for experimental study. The dipoles noted in figure 8 were used to define the positions, with spatial averaging performed last. The experimental spectra for core nanoparticles with and without a gold shell are also plotted for comparison. These calculations assume constant transition probabilities in the Yb^{3+}/Er^{3+} system, as a result of interposing a 60 nm thick undoped buffer layer between the doped upconverting center and the gold shell. Thus, the calculated enhancement must be due to electromagnetic effects. It must come from the emission process, since the excitation light, enhanced by plasmons, is the same for all emission. The electromagnetic effects, shown by the calculation, do a good job of explaining the enhancement of the green emission, suggesting that the undoped buffer layer is thick enough for this wavelength. However, the electromagnetic effects overestimate the enhancement of the red emission, suggesting that either the (Ohmic) losses in the gold are higher than expected or that some modification of the rates in the Yb^{3+}/Er^{3+} system reduced the red emission. We suspect that the edges of the doped core are close enough to the metal that the red (longer wavelength) optical processes are impacted (sped up) by the interaction. These Yb^{3+}/Er^{3+} system changes would be more important in smaller particles and those without an undoped buffer layer.

Maximum emitted power will be attained when there is minimum electric field in the metal layer, when the emitted wavelength is resonant in the cavity with a node at the edges. There is good evidence for such a resonance, shown in figure 10, for 540 nm driven at the edge of the doped region, but not driven at the center, and not for 660 nm at either position, based upon the cavity size and index, resonance and loss in figure 7, and an examination of the magnitude and spatial dependence of the electric field just under the gold layer. The figure shows a nicely defined mode pattern for the 540 nm emission, but a less organized, non-modal distribution for the 660 nm emission. Taking the cavity just inside the gold shell, 490 nm, and cavity index of refraction 1.6, we find an optical size of 780 nm, which agrees reasonably well with the excitation resonance peak observed in figure 2 at 12 min. This size fits 1.5 wavelengths at 520 nm, which is very close to the green emission at 540 nm, so it is also resonant. The red emission at 660 nm is far from resonant. This can also be seen in figure 7, where the maxima (near 540 nm) in the emission ratio are resonant and minima (near 650 nm) are not. The ~7 times larger scale of the maximal field near the gold for 660 nm documents the higher dissipation (loss in the gold layer due to the field). When the dipole is near the center, the 540 nm light also displays a mode pattern, but with maximum field at the center (the node of the 540 mode above) and an antinode at the edges. Thus, the dipoles near the doped core edge are the dominant contributors to the green/red emission ratio. The detailed wavelength dependence for several dipole points shown in figure 7 is consistent with the above

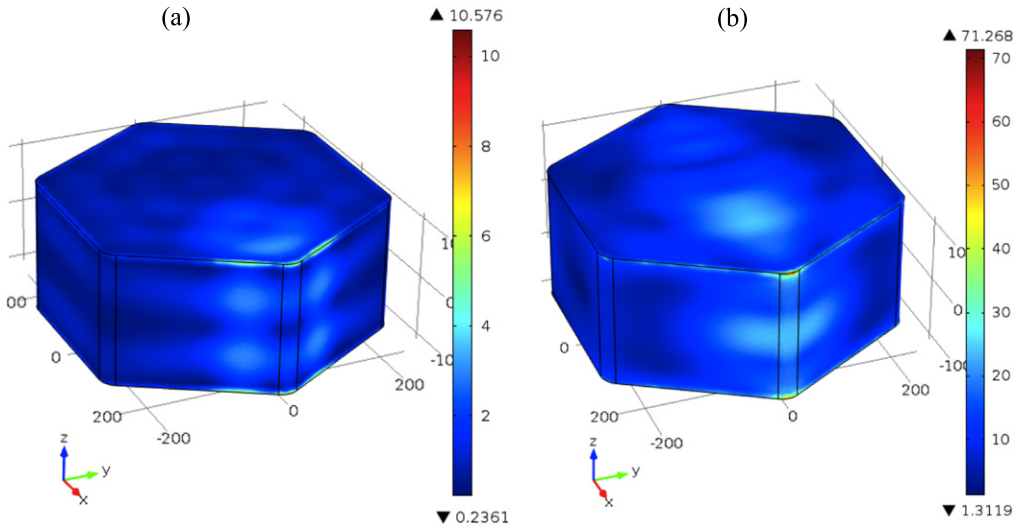

Figure 10. The magnitude of the electric field emitted by a dipole of unit strength near the apex of the doped core region is shown at the surface of the gold layer: (a) emission at 540 nm, (b) emission at 660 nm.

discussion: the dipole at the center has little emission wavelength dependence, whereas those at the edge have a larger ratio.

Conclusion

In summary, we have synthesized upconverting gold-shell nanoparticles, demonstrated enhanced overall emission, and shown enhancement of the green compared to the red emission at the single particle level. Our absorption spectrum demonstrated the plasmon resonant coupling of the gold shell to the upconverting core. We also show that the electric field distribution and hence excitation enhancement is affected when the nanoparticles are aggregated. Our finite element calculations reinforce our experimental observations that the upconverting cores are indeed plasmonicly coupled to the gold nanostructures and experience electric field enhancement within the cores. We also show that the regions near the edge of the doped cores are responsible for most of the green/red emission ratio increase. Hence, the excitation enhancement is optimal with excitation normal to the hexagonal face, with polarization aligned diagonally to the hexagonal corners and also perpendicular to the edges.

Acknowledgment

We acknowledge support from NSF CBET 1067508 and discussions with Dr Robert Riehn.

References

[1] Lichtman J W and Conchello J A 2005 *Nat. Methods* **2** 910–9
[2] Stokes G G 1852 *Phil. Trans. R. Soc.* A **142** 463–562
[3] Gu M, Gan X, Kisteman A and Xu M G 2000 *Appl. Phys. Lett.* **77** 1551–3
[4] Giloh H and Sedat J 1982 *Science* **217** 1252–5
[5] Denk W, Strickler J and Webb W 1990 *Science* **248** 73–6
[6] Helmchen F and Denk W 2005 *Nat. Methods* **2** 932–40
[7] Frangioni J V 2003 *Curr. Opin. Chem. Biol.* **7** 626–34
[8] Chen W, Joly A G and McCready D E 2005 *J. Chem. Phys.* **122** 224708
[9] Blanton S A, Dehestani A, Lin P C and Guyot-Sionnest P 1994 *Chem. Phys. Lett.* **229** 317–22
[10] Lakowicz J R, Gryczynski I, Piszczek G and Murphy C J 2002 *J. Phys. Chem.* B **106** 5365–70
[11] Su Z P, Teo K L, Yu P Y and Uchida K 1996 *Solid State Commun.* **99** 933–6
[12] Kammerer C, Cassabois G, Voisin C, Delalande C, Roussignol P and Gerard J M 2001 *Phys. Rev. Lett.* **87** 207401
[13] Simon Y C, Bai S, Sing M K, Dietsch H, Achermann M and Weder C 2012 *Macromol. Rapid Commun.* **33** 498–502
[14] Sun Y F, Chen Z Y, Zhu L, Xu S H, Wu R T and Cui Y P 2013 *Color. Technol.* **129** 165–72
[15] Rumi M *et al* 2000 *J. Am. Chem. Soc.* **122** 9500–10
[16] Naccache R, Vetrone F, Speghini A, Bettinelli M and Capobianco J A 2008 *J. Phys. Chem.* C **112** 7750–6
[17] Wang X F, Xiao S G, Bu Y Y, Yang X L and Ding J W 2008 *Opt. Lett.* **33** 2653–5
[18] Auzel F 2004 *Chem. Rev.* **104** 139–73
[19] Wang F, Han Y, Lim C S, Lu Y H, Wang J, Xu J, Chen H Y, Zhang C, Hong M H and Liu X G 2010 *Nature* **463** 1061–5
[20] Priyam A, Idris N M and Zhang Y 2012 *J. Mater. Chem.* **22** 960–5
[21] Lim S F, Riehn R, Ryu W S, Khanarian N, Tung C-K, Tank D and Austin R H 2006 *Nano Lett.* **6** 169–74
[22] Lim S F, Riehn R, Tung C-K, Ryu W S, Zhuo R, Dalland J and Austin R H 2009 *Nanotechnology* **20** 405701
[23] Wu S, Han G, Milliron D J, Aloni S, Altoe V, Talapin D V, Cohen B E and Schuck P J 2009 *Proc. Natl. Acad. Sci. USA* **106** 10917–21
[24] Faris G W, Wright W H, Pati S, Schneider L V and Zarling D A 1996 Upconverting reporters for biomedical diagnostics: applications in antibody and DNA detection *Optical Society of America* ed E Sevick-Muraca and D Benaron (Washington, USA: Optical Society of America) DR2

[25] van de Rijke F, Zijlmans H, Li S, Vail T, Raap A K, Niedbala R S and Tanke H J 2001 *Nat. Biotechnol.* **19** 273–6
[26] Zijlmans H J M A A, Bonnet J, Burton J, Kardos K, Vail T, Niedbala R S and Tanke H J 1999 *Anal. Biochem.* **267** 30–6
[27] Hampl J, Hall M, Mufti N A, Yao Y-m M, MacQueen D B, Wright W H and Cooper D E 2001 *Anal. Biochem.* **288** 176–87
[28] Zuiderwijk M, Tanke H J, Sam Niedbala R and Corstjens P L 2003 *Clin. Biochem.* **36** 401–3
[29] Corstjens P, Zuiderwijk M, Brink A, Li S, Feindt H, Niedbala R S and Tanke H 2001 *Clin. Chem.* **47** 1885–93
[30] Corstjens P L A M, Zuiderwijk M, Nilsson M, Feindt H, Sam Niedbala R and Tanke H J 2003 *Anal. Biochem.* **312** 191–200
[31] Zeng J H, Su J, Li Z H, Yan R X and Li Y D 2005 *Adv. Mater.* **17** 2119–23
[32] Wang L and Li Y 2006 *Chem. Commun.* **24** 2557–9
[33] Kuningas K, Rantanen T, Karhunen U, Lövgren T and Soukka T 2005 *Anal. Chem.* **77** 2826–34
[34] Yi G, Lu H, Zhao S, Ge Y, Yang W, Chen D and Guo L-H 2004 *Nano Lett.* **4** 2191–6
[35] Idris N M, Gnanasammandhan M K, Zhang J, Ho P C, Mahendran R and Zhang Y 2012 *Nat. Med.* **18** 1580–5 (www.nature.com/nm/journal/v18/n10/abs/nm.2933.html#supplementary-information)
[36] Zhang P, Steelant W, Kumar M and Scholfield M 2007 *J. Am. Chem. Soc.* **129** 4526–7
[37] Guo Y, Kumar M and Zhang P 2007 *Chem. Mater.* **19** 6071–2
[38] Ungun B, Prud'homme R K, Budijon S J, Shan J, Lim S F, Ju Y and Austin R 2009 *Opt. Express* **17** 80–6
[39] Qian H S, Guo H C, Ho P C, Mahendran R and Zhang Y 2009 *Small* **5** 2285–90
[40] Shan G B, Weissleder R and Hilderbrand S A 2013 *Theranostics* **3** 267–74
[41] Ivanova S and PellÈ F 2009 *J. Opt. Soc. Am.* B **26** 1930–8
[42] Shalav A, Richards B S and Green M A 2007 *Sol. Energy Mater. Sol. Cells* **91** 829–42
[43] van der Ende B M, Aarts L and Meijerink A 2009 *Phys. Chem. Chem. Phys.* **11** 11081–95
[44] de Wild J, Rath J K, Meijerink A, van Sark W G J H M and Schropp R E I 2010 *Sol. Energy Mater. Sol. Cells* **94** 2395–8
[45] Zou W Q, Visser C, Maduro J A, Pshenichnikov M S and Hummelen J C 2012 *Nat. Photonics* **6** 560–4
[46] Liang L L *et al* 2013 *Adv. Mater.* **25** 2174–80
[47] Longmire M, Choyke P L and Kobayashi H 2008 *Nanomedicine* **3** 703–17
[48] Payne S A, Chase L L, Smith L K, Kway W L and Krupke W F 1992 *IEEE J. Quantum Electron.* **28** 2619–30
[49] Dou Q and Zhang Y 2011 *Langmuir: ACS J. Surf. Colloids* **27** 13236–41
[50] Dhananjaya N, Nagabhushana H, Nagabhushana B M, Rudraswamy B, Shivakumara C and Chakradhar R P S 2011 *J. Alloys Compd.* **509** 2368–74
[51] Zhao C, Kong X, Liu X, Tu L, Wu F, Zhang Y, Liu K, Zeng Q and Zhang H 2013 *Nanoscale* **5** 8084–9
[52] Cheng Q, Sui J and Cai W 2012 *Nanoscale* **4** 779–84
[53] Chen G, Liang H, Liu H, Somesfalean G and Zhang Z 2009 *Opt. Express* **17** 16366–71
[54] Chen D, Yu Y, Huang F, Yang A and Wang Y 2011 *J. Mater. Chem.* **21** 6186–92
[55] Liu Q, Sun Y, Yang T, Feng W, Li C and Li F 2011 *J. Am. Chem. Soc.* **133** 17122–5
[56] Dong B, Cao B, He Y, Liu Z, Li Z and Feng Z 2012 *Adv. Mater.* **24** 1987–93
[57] Zhou B, Tao L, Tsang Y H and Jin W 2013 *J. Mater. Chem.* C **1** 4313–8
[58] Kulakovich O, Strekal N, Yaroshevich A, Maskevich S, Gaponenko S, Nabiev I, Woggon U and Artemyev M 2002 *Nano Lett.* **2** 1449–52
[59] Jin Y and Gao X 2009 *Nat. Nanotechnology* **4** 571–6 (www.nature.com/nnano/journal/v4/n9/suppinfo/nnano.2009.193_S1.html)
[60] Shimizu K T, Woo W K, Fisher B R, Eisler H J and Bawendi M G 2002 *Phys. Rev. Lett.* **89** 117401
[61] Pompa P P, Martiradonna L, Torre A D, Sala F D, Manna L, De Vittorio M, Calabi F, Cingolani R and Rinaldi R 2006 *Nat. Nanotechnology* **1** 126–30
[62] Bardhan R, Grady N K, Ali T and Halas N J 2010 *ACS Nano* **4** 6169–79
[63] Halas N J 2010 *Nano Lett.* **10** 3816–22
[64] Schietinger S, Aichele T, Wang H-Q, Nann T and Benson O 2009 *Nano Lett.* **10** 134–8
[65] Paudel H P, Zhong L, Bayat K, Baroughi M F, Smith S, Lin C, Jiang C, Berry M T and May P S 2011 *J. Phys. Chem.* C **115** 19028–36
[66] Li Z Q, Li X D, Liu Q Q, Chen X H, Sun Z, Liu C, Ye X J and Huang S M 2012 *Nanotechnology* **23** 025402
[67] Sun Q-C, Mundoor H, Ribot J C, Singh V, Smalyukh I I and Nagpal P 2013 *Nano Lett.* **14** 101–6
[68] Malta O L, Santacruz P A, Desa G F and Auzel F 1985 *J. Lumin.* **33** 261–72
[69] Malta O L, Santacruz P A, Desa G F and Auzel F 1987 *J. Solid State Chem.* **68** 314–9
[70] Gargas D J *et al* 2014 *Nat. Nanotechnology* **9** 300–5 (www.nature.com/nnano/journal/v9/n4/abs/nnano.2014.29.html#supplementary-information)
[71] Li Z Q, Chen S, Li J J, Liu Q Q, Sun Z, Wang Z B and Huang S M 2012 *J. Appl. Phys.* **111** 014310–7
[72] Lassiter J B, Aizpurua J, Hernandez L I, Brandl D W, Romero I, Lal S, Hafner J H, Nordlander P and Halas N J 2008 *Nano Lett.* **8** 1212–8
[73] Neretina S, Qian W, Dreaden E C, El-Sayed M A, Hughes R A, Preston J S and Mascher P 2009 *Nano Lett.* **9** 1242–8
[74] Suyver J F, Aebischer A, Garcia-Revilla S, Gerner P and Gudel H U 2005 *Phys. Rev.* B **71** 125123
[75] Suyver J F, Grimm J, van Veen M K, Biner D, Kramer K W and Gudel H U 2006 *J. Lumin.* **117** 1–12
[76] Johnson P B and Christy R W 1972 *Phys. Rev.* B **6** 4370–9
[77] Aspnes D E 1982 *Am. J. Phys.* **50** 704–9